J. Phys. Chem. A **2005,** *109,* 421−430

Porphyrin Distortion from Resonance Raman Intensities of Out-of-Plane Modes: Computation and Modeling of *N*-Methylmesoporphyrin, a Ferrochelatase Transition State Analog

Andrzej A. Jarzęcki[†] and Thomas G. Spiro*

Department of Chemistry, Princeton University, Princeton New Jersey 08544

Received: July 6, 2004; In Final Form: October 8, 2004

Resonance Raman spectra of porphyrins are computed with DFT/CIS methodology to monitor out-of-plane distortions. A framework is established for assessing protein-induced distortion of porphyrin bound to a ferrochealatase antibody. Tests on undistorted porphyrins give good agreement with the experimental intensity pattern of in-plane modes for free-base porphine (FBP) and mesorporphyrin IX free base (MP). The computed spectrum of *N*-methylmesoporphyrin (NMP), in which the methyl-substituted pyrrole ring is tilted 32° from the mean porpyrin plane, also gives reasonable agreement with experiment and reveals activation of out-of-plane (oop) vibrational modes. To model oop distortions systematically, an artificial molecule, FBP-X_8, was constructed, in which the H atoms attached to the FBP pyrrole C_b atoms are replaced by heavy substituents, as in physiological porphyrins. Oop mode enhancements are computed for FBP-X_8 by displacing it along the canonical distortion coordinates: doming, saddling, ruffling and waving. When FBP-X_8 is constrained to the NMP porphyrin geometry, normal coordinate decomposition reveals significant contributions also from modes higher in frequency than the canonical modes, and they contribute importantly to the computed RR intensities. NMP-constrained FBP-X_8 gives a reasonable facsimile of the NMP RR spectrum, but better results are obtained with a full computation of MP, constrained in the same way; thus the physiological substituents have significant influence on the RR spectra, over and above their effective masses. Attention focuses on a mode analogous to γ_{15} in 4-fold symmetric porphyrins, which is a kind of saddling mode. This mode is selectively enhanced in NMP-constrained MP; a corresponding RR band is induced upon binding MP to a ferrochelatase antibody.

Introduction

Out-of-plane distortions of the porphyrin macrocycle are of interest because of their possible functional roles in heme- and chlorophyll-containing proteins.[1] A well-defined role for porphryin distortion is implicated in the chelatase enzymes,[2−4] which insert metal ions into the porphyrin, probably by tilting the pyrrole rings to expose the electron pairs of the coordinating N atoms to the incoming metal.[5,6] N-alkylated porphyrins, in which the steric requirements of the alkyl goup force pyrrole tilting,[7] are strong ferrochelatase inhibitors,[8] and antibodies raised to *N*-methylmesoporphyrin IX (NMP) are found to catalyze metal ion insertion into mesoporphyrin IX free-base (MP).[9]

Porphyrin distortion can be monitored sensitively via the resonance Raman spectrum. Distortion-induced alterations in the ring kinematics as well as in the electronic structure can shift skeletal mode frequencies of the porphyrin.[10−14] In addition, RR intensity is induced for out-of-plane (oop) vibrational modes,[12] which are unobserved in planar porphyrins because the resonant $\pi-\pi^*$ electronic transitions are polarized in the porphyrin plane. Out-of-plane distortions project a component of the oop modes onto the in-plane electronic excitation, thereby inducing RR intensity. These effects have been investigated systematically in nickel porphyrins, which are distorted to accommodate the short Ni−N(pyrrole) bonds.[15] Skeletal mode frequency shifts have been documented, as have oop mode activations.[10−14]

Nickel porphyrins have also served to test methods for computing RR spectra through DFT-based force fields,[16−19] and through evaluation of excited state displacements or gradients.[17−19] The experimental intensity pattern was predicted quite well, including the activation of oop modes.[17,18] In the present work, we extend these results by establishing a framework for porphyrins constrained by external forces to be nonplanar. The objective is to model the oop mode activation when porphyrins are distorted upon binding to proteins. Application of this framework to the distortion of mesoporphyrin by a ferrochelatase antibody is reported elsewhere.[20]

Methods

Raman Intensities. The RR intensity can be evaluated from the computationally determined displacement, along the *k*th vibrational mode, of the minimum in the resonant excited state potential surface from the ground state, Δ_k, together with the Kramers−Kronig transform of the electronic absorption band,[21,22] $\Phi(\omega_L)$.

$$I_k \propto \omega_L(\omega_L - \omega_k)^3 \Delta_k^{\,2} |\Phi(\omega_L) - \Phi(\omega_L - \omega_k)|^2 \qquad (1)$$

where ω_L is the frequency of the incident light and ω_k is the vibrational frequency. The experimentally determined Kramers−Kronig transform scaling factor, $|\Phi(\omega_L) - \Phi(\omega_L-\omega_k)|^2$ affects the computed RR intensity pattern by suppressing the intensity of lower frequency modes relative to the higher frequency

---

* Corresponding author. E-mail: spiro@princeton.edu.

[†] Current address: Department of Chemistry, Brooklyn College, The City University of New York, Brooklyn, NY 11210.

10.1021/jp0470142 CCC: $30.25

modes;[17,18] this results from cancellation between the $\Phi(\omega_L)$ and $\Phi(\omega_L-\omega_k)$ terms as the scattered frequency approaches the incident frequency. Additionally, the transform procedure directly allows for modeling of the changes in the RR intensity pattern as a function of the experimental excitation energy. In the present work we have omitted this factor, because we are interested in the relative intensities of bands in a relatively confined spectral region, for porphyrin excitations near the strong Soret band ($B_{x,y}$ electronic transitions).

When the absorption band is diffuse, and the laser excitation is significantly below the electronic transition energy, eq 1 can be approximated[23,24] by

$$I_k \propto \omega_L(\omega_L-\omega_k)^3\Delta_k^{\,2}\omega_k^{\,2} \qquad (2)$$

which in the time domain is equivalent to the short-time propagation of the ground state vibrational wave packet on the resonant state potential energy surface.[25,26] In this approximation the dependence of the relative RR intensities on the laser frequency, ω_L, is practically negligible because the ratio $(\omega_L-\omega_k)^3/(\omega_L-\omega_{k'})^3$ is close to unity; the RR intensity pattern depends only by the dimensionless displacement of the potential energy surface minima along the normal modes, Δ_k. The displacement is related to the structural change, ΔX_j, in the internal coordinates upon excitation of the molecule into the relevant excited state or equivalently, to the gradient in the Franck–Condon region.[25,26]

$$\Delta_k \propto \omega_k^{\,1/2}\sum_{j=1}^{3N-6} L_{k,j}^{\;-1}\Delta X_j \propto -\frac{1}{\omega_k}\left(\frac{\partial E}{\partial Q_k}\right)\left(\frac{\partial Q_k}{\partial \Delta_k}\right) \qquad (3)$$

where $L_{k,j}^{\;-1}$ are the elements of the **L** inverse matrix determined from the solution of the ground state normal-mode eigenvalue problem, and $(\partial E/\partial Q_k)$ is the energy gradient along the normal coordinate. The gradient interpretation of resonance Raman experiments is especially suitable for computational modeling, because the estimated vertical gradients on the resonant excited state are fundamental molecular entities that connect excited wave packet motion to classical mechanics and provide a simple physical and intuitive basis for the Raman scattering. When the normal coordinates are related to dimensionless coordinates by $(\partial Q_k/\partial\Delta_k) = (h/2\pi\mu_k\omega_k)^{1/2}$, where h is the Planck constant and μ_k is the effective mass of kth vibrational mode, eq 2 can be rewritten as

$$I_k \propto \omega_L(\omega_L-\omega_k)^3\frac{1}{\mu_k\omega_k}\left(\frac{\partial E}{\partial Q_k}\right)^2 \qquad (4)$$

which directly relates the RR intensity to the computed energy gradient on the resonant state at the vertical excitation.

Ground State Geometry and Force Field. Calculations of the ground state geometries, harmonic force constants, and frequencies were performed using density functional theory with a nonlocal hybrid functional, the Becke three parameter exchange and Lee–Young–Parr correlation functionals (B3LYP), and moderate 6-31G* basis functions, as implemented in the Gaussian 98 suite of programs.[27] To improve the quality of computed frequencies and normal modes, the scaled quantum mechanical (SQM) refinement of DFT force constants was employed, using transferable scaling factors.[28,29] The SQM treatment has been successfully applied in vibrational analysis of porphyrin systems,[16,30] giving confidence in the predicted ground state vibrational modes.

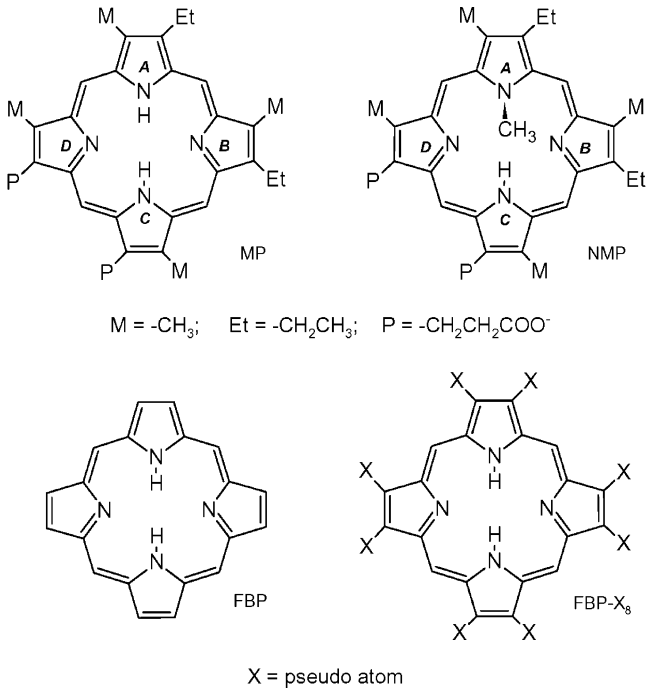

Figure 1. Structural diagrams for the molecules in this study.

Excited State Gradients. RR intensity prediction requires accurate estimation of excited state gradients in the Franck–Condon region, although the excitation energies themselves need not be accurately computed. Satisfactory intensities were earlier obtained for Ni-porphyrins using the semiempirical ZINDO approximation for the B and Q excited states.[17−19] ZINDO is specifically paramatrized for metalloporphyrins, and we find better results for free-base poprhyrins using the computationally efficient CIS (configuration interaction with single excitations) method[31] to model the excited states. Its efficacy was earlier demonstrated for the UVRR intensities of imidazole.[32] In that study, the moderate basis set functions 6-31G* gave good results, and the even smaller basis set functions 3-21G* were satisfactory. In the present work, we used 6-31G* functions for free-base porphine (FBP), and 3-21G* functions for the larger substituted porphyrins (MP and NMP).

The CIS excitations were limited to a four-orbital window that dominates the visible and near-ultraviolet spectra of porphyrins, i.e., two HOMO and two LUMO orbitals, with a $\pi^2\pi^2\ \pi^{*0}\pi^{*0}$ ground state electronic configuration.[33,34]

Gradient Corrections. Because the RR intensity computation requires the excited state gradient at the equilibrium geometry of the ground state, it is essential to take into account the different levels of theory, DFT vs CIS, which are used for the ground and excited states. CIS involves excitations from a Hartree–Fock (HF) potential, which does not produce the same ground state equilibrium geometry as does DFT. Consequently, the shift from the DFT to the HF potential must be taken into account in evaluating the CIS excited state gradient, as illustrated in Figure 2a.

The corrected gradient is obtained via

$$\left(\frac{\partial E}{\partial Q_k}\right)_{\rm corr} = \left(\frac{\partial E}{\partial Q_k}\right)_{\rm CIS} - \left(\frac{\partial E}{\partial Q_k}\right)_{\rm HF} \qquad (5)$$

where subscripts “CIS” and “HF” denote the calculated CIS and HF gradients on corresponding potential energy surfaces along a normal mode k at the DFT ground state equilibrium geometry, and the subscipt “corr” indicates the corrected gradient.

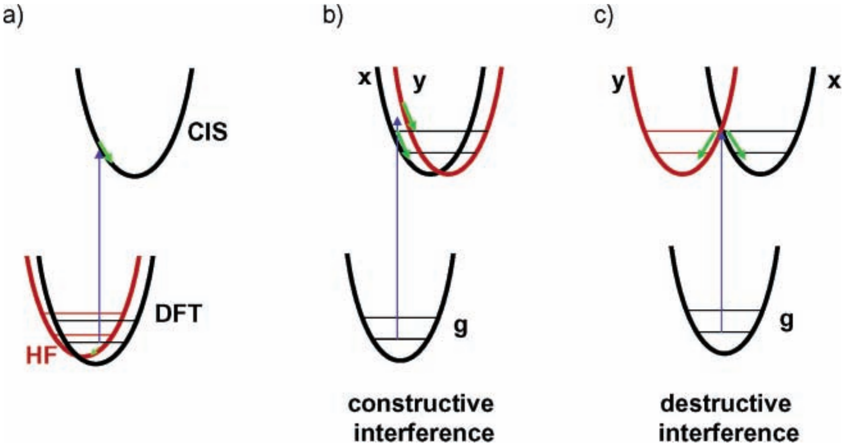

Figure 2. Diagram illustrating (a) the computed gradient correction required to reconcile DFT-ground and CIS-excited state potential surfaces, and (b) and (c) the possibility of constructive and destructive interferences from close-lying excited states (B_x and B_y) to the Raman amplitude.

We found that the gradient correction has large effects on the computed intensities, especially for low-frequency modes.

Excitation to Nearly Degenerate Electronic States. An additional complication for the RR intensity is near-degeneracy among the pophyrin excited states. In the limit of 4-fold symmetry, the excited states are exactly degenerate (E-symmetry), but the two protons on the free-base porphyrin pyrrole rings (Figure 1) split the excitations, into *x*- and *y*-polarized components. The asymmetrical disposition of peripheral substituents (and of polar residues in proteins), can also lift the degeneracy, although the effects are smaller.

Because the excited state splittings are not large, the RR intensities are subject to interferences between the closely spaced electronic components. Their resonant contributions add or subtract at the amplitude level, as illustrated in Figure 2b,c. An "effective gradient" for a given mode can be expressed as

$$\left(\frac{\partial E}{\partial Q_k}\right)_{\rm eff} = w_x\left(\frac{\partial E}{\partial Q_k}\right)_x + w_y\left(\frac{\partial E}{\partial Q_k}\right)_y \qquad (6)$$

where w_x and w_y are the weighting factors for the computed gradients of the x- and y-polarized near-resonant states. In the limit of 4-fold symmetry, the two terms in eq 6 are equal, and the treatment reduces to that of a single resonant transition (as in the cases of Ni-porphine and Ni-tetraphenyl porphine).[17−19] In general, however, the weighting factors depend on the

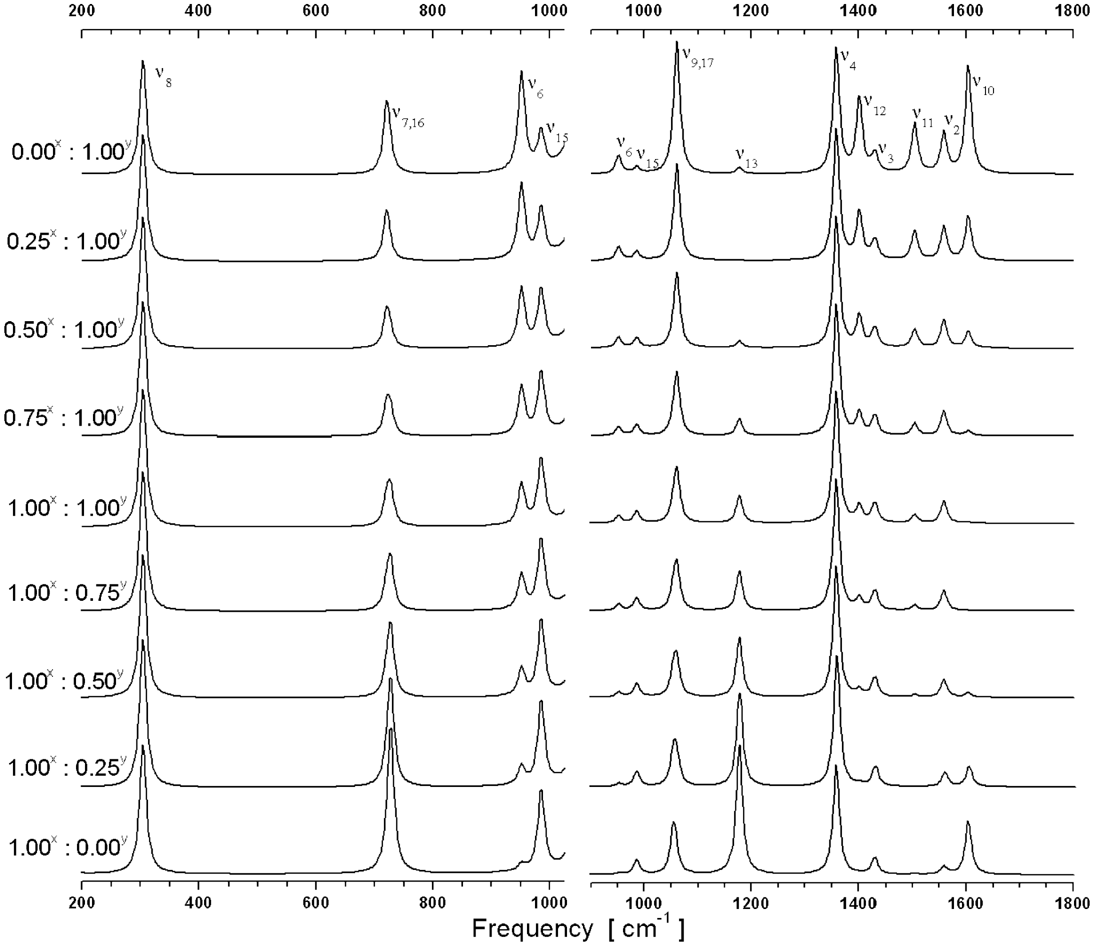

Figure 3. Effect on the computed FBP RR spectrum of varying the weighting of B_x and B_y contributions to the Raman amplitude (eq 6).

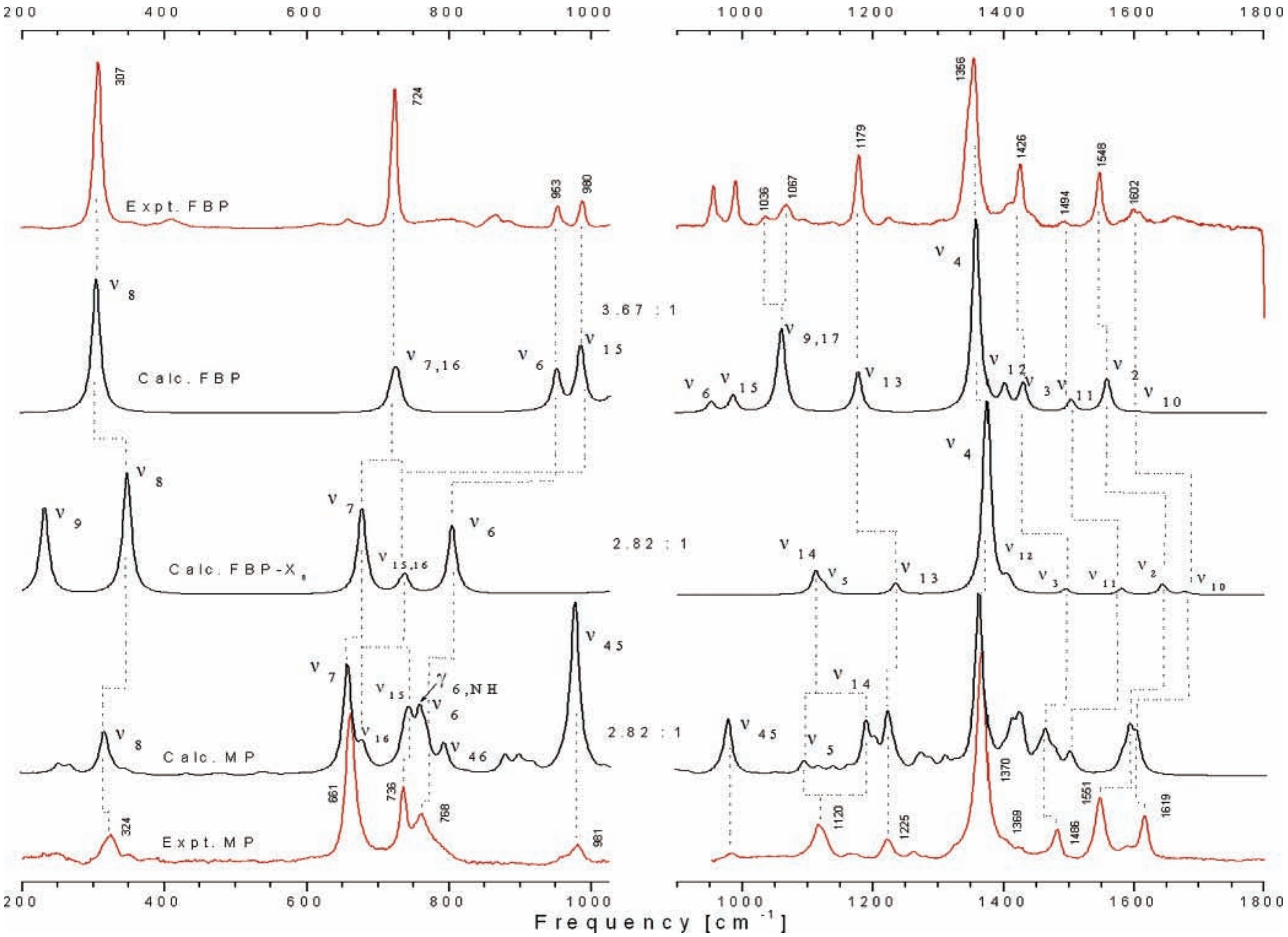

Figure 4. Comparison of experimental RR spectra for FBP (top) and MP (bottom) with computed spectra. The intensity of bands in the lower frequency regions were expanded by the indicated ratios for clarity.

TABLE 1: Average Values of Selected Bond Lengths (Å) and Angles (deg) for Porphyrin Rings

	exp[a] FBP	calc FBP	calc MP	exp[b] NMP[c]	calc NMP[c]
Ca−N	1.379	1.368	1.368	1.367	1.370
Ca−Cb	1.442	1.448	1.458	1.449	1.458
Cb-Cb	1.358	1.364	1.376	1.331	1.376
Ca−Cm	1.382	1.397	1.398	1.403	1.401
C−N				1.477	1.467
Ca−N−Ca	107.3	108.1	108.0	107.7	107.7
N−Ca−Cm	125.1	125.5	125.1	125.9	125.0
Ca−Cm−Ca	127.1	127.1	127.9	125.2	128.2
Ca−Cb-Cb	107.5	107.1	106.7	107.6	106.7

[a] X-ray data from ref 44. [b] Data for *N*-methyltetra(*p*-bromophenyl)porphyrin from ref 43. [c] The tilt out of the mean plane of the ring A is observed at 28.9 and calculated at 31.8 degrees.

strengths, widths, and energies of the two transitions, and on the off-resonant tuning of the laser. The weighting factors can be determined by separate application of the Kramers−Kronig transform (eq 4) to the two transitions. However, because we are interested only in the relative intensities of the various porphyrin modes, we found it convenient simply to treat the ratio of the weighting factors as an empirical parameter, after computation of the B_x and B_y gradients via CIS. Figure 3 illustrates how computed RR spectra for free-base porphine depend on the relative weighting factors. In the limit of zero contribution for either the B_x or B_y gradients, the relative intensities differ considerably. However, in the neighborhood of equal contributions, the relative intensities vary only slowly. We found that equal weighting gave best agreement with experimental spectra (see below) and adopted a 1:1 ratio in all the calculations. The error introduced by this approximation is less than the errors intrinsic to the CIS gradients themselves, as judged by the comparison with experiment.

Experimental Spectra

Solutions of MP and NMP (Midcentury Chemicals) were prepared by dissolution in aqueous NH_4OH with added Triton-X100 (2%) and adjusted with tris-HCl buffer to a pH of 8.0 and a porphyrin concentration of 50 μM. FBP (Midcentury Chemicals) was dissolved in dimethylformamide to a similar concentration. The solutions were purged with N_2 prior to Raman excitation, to avoid photooxidation.

Raman spectra were obtained in spinning NMR tubes with 135° backscattering from a 406.7 nm Kr^+ laser, with 10−15 mW at the sample. Spectra were collected for ∼15 min with a Spex 1877 triple monochromator (2400 grooves/mm grating) equipped with a diode array detector.

Results and Discussion

In-Plane RR Intensities. *Free-Base Porphine (FBP).* To assess the accuracy of CIS gradients for porphyrins, we compared computed and experimental RR spectra (407 nm excitation) for FBP (Figure 4, top spectra). DFT-SQM has previously been shown to give an excellent account of the

TABLE 2: Predicted In-Plane Mode Frequencies and RR Intensities for the FBP-X_8 Model, and Mode Correlation with NiOEP

		NiOEP						NiOEP					NiOEP		FBP-X_8	
symm D_{4h}/D_{2h}	assign ν_i	exp[a]	SQM-DFT[b]	FBP-X_8	I_{RR}[c]	symm D_{4h}/D_{2h}	assig ν_i	exp[a]	SQM-DFT[b]	FBP-X_8	symm D_{4h}/D_{2h}	assign ν_i	exp[a]	SQM-DFT[b]		
	NH			3376	135.36		NH			758	$E_u/B_{2u(3u)}$	36	[3040]	3085	3056	3056
A_{1g}/A_g	1	[3041]		3056	9.48	A_{2g}/B_{1g}	19	1603	1602	1589		37	[1637]	1609	1678	1639
	2	1602	1604	1644	5.66		20	1393	1395	1433		38	1604	1570	1585	1510
	3	1520	1517	1496	2.88		21	1307	1317	1329		39	1501	1483	1511	1454
	4	1383	1386	1374	**100.00**		22	1121	1122	1205		40	1396	1371	1478	1415
	5	1138	1138	1125	4.04		23	1058	1129	1137		41	[1346]	1396	1261	1393
	6	804	796	804	3.24		24	597	906	604		42	1231	1234	1231	1201
	7	674	665	677	**4.05**		25	551	604	582		43	1153	1132	1174	1148
	8	343	341	348	5.74		26	[243]	558	260		44	1133	1146	1109	1105
	9	274	286	231	4.12	B_{2g}/B_{1g}	27	[3041]	3085	3056		45	996	983	946	962
B_{1g}/A_g	10	1655	1658	1679	1.53		28	1483	1483	1482		46	927	908	818	816
	11	1577	1576	1581	3.25		29	1407	1407	1490		47	[791]	747	719	719
	12	[1330]	1400	1406	6.77		30	1159	1158	1224		48	605	693	632	637
	13	1220	1219	1235	5.87		31	1015	1013	1006		49	544	596	530	522
	14	1131	1132	1112	11.79		32	938	920	936		50	[358]	506		
	15	751	753	738	0.82		33	493	652	518		51	328	331	337	341
	16	740	678	731	0.23		34	197	525	222		52	263	304	251	262
	17	305	320	316	0.00		35	144	260	91		53	212	349	189	192
	18	168	192	130	0.07							NH	bend		1410	
												NH	stretch			3338

[a] From ref 39 (empirical force field predictions for unobserved models in square brackets). [b] From ref 38. [c] RR intensities, relative to ν_4, computed as described in the text, with 1:1 weighting of B_x and B_y contributions to the resonant amplitude.

experimentally observed FBP frequencies,[35,36] and we adopted the published DFT-SQM force field. The optimized structure is flat, and the bond distances and angles accord well with experiment (Table 1).

CIS gradients are seen to reproduce the relative RR intensities satisfactorily (see refs 35 and 36 for assignments). The ν_4 and ν_8 bands are correctly predicted to be the most intense bands in the high- and low-frequency regions. The intensity pattern of the remaining bands is close to the observed pattern, although there are minor discrepancies. Thus ν_2, ν_3, and ν_7 are somewhat low, whereas ν_9 is too high, in relation to ν_4.

Model for Porphyrins with C_b-C Substituents: FBP-X_8. The porphine RR spectrum differs significantly from the spectra of physiological prophyrins, because the latter all have heavy substituents (alkyl, vinyl, or formyl) in place of hydrogen. The substituents contibute to the normal modes and influence RR frequencies and intensities. Inclusion of these substituents substantially increases the size and complexity of the calculation, and we sought a simpler model that would still capture the mass effect of the heavy substituents and would permit systematic exploration of distortion modes. We placed a set of eight carbon pseudo-atoms, X, at the C_b positions, and gave them an effective mass of 12.75 amu, after a series of trial computations with different masses. The FBP structure and force field were otherwise unchanged.

Table 2 lists computed frequencies and relative RR intensities for the FBP-X_8 in-plane modes (ν_i). The frequencies are compared with the recently reported DFT-SQM porphyrin skeletal frequencies for Ni octaethylporphyrin (NiOEP)[37,38] along with the observed RR and IR values.[39] NiOEP is a thoroughly studied physiological heme analogue, which has approximate 4-fold symmetry; its skeletal frequencies are conveniently classifiable within the D_{4h} point group. FBP-X_8 has D_{2h} symmetry, but the D_{4h} parentage is readily apparent in the excellent correlations observed with NiOEP. Lowering the symmetry to D_{2h} splits the E_u modes into B_{2u} and B_{3u} components, but the predicted splittings are small in most cases.

There are, of course, differences occasioned by the replacement of Ni with two protons, the most obvious of which are the appearance of two NH stretching and two NH bending modes, in place of the degenerate (E_u) Ni−N stretch. Significant mode frequency differences are also predicted, especially in the low-frequency region, where the absence of a metal at the center of the cavity lowers the in-plane bending frequencies. The biggest effects are seen for the ν_{26} and ν_{34} modes, which are predicted to lie 300 cm^{-1} lower than in NiOEP. Overall, however, the match to NiOEP is very good, validating the use of FBP-X_8 as a model.

The FBP-X_8 modes were helpful in assigning the modes of mesoporphyrin IX free base (MP; see Figure 1), which was included in this study and is the focus of our paper on an antibody with ferrochelatase activity.[20] Because MP has only a plane of symmetry, correlation of the computed modes with the parent D_{4h} modes is not obvious, especially in the low-frequency region, where substituent deformations play a significant role. However, the computed spectrum (Figure 4), shows clear correspondences with that of FBP-X_8, and with the MP experimental spectrum, so that assignments can be made with confidence for the stronger bands listed in Table 4. We note that MP can have two trans isomers, depending on the disposition of the protons relative to the substituents, but the computation gave essentially the same results for both of them.

In the region above 1400 cm^{-1}, the computed frequencies are systematically higher for FBP-X_8 (Table 4) than for FBP itself or for MP. These modes are known to be sensitive to the porphyrin core size; the larger the core, the lower the frequencies.[40] Geometry optimization in the DFT calculations (Table 1) yielded a slightly larger core for MP than for FBP (4.147 vs 4.157 Å diagonal N···N distance) so that lower frequencies would be expected for MP. However, mixing with substituent coordinates evidently raises the skeletal mode frequencies; this is evident in the upshifts seen for FBP-X_8 relative to FBP, because the FBP skeleton was held fixed when the X substituents were added. Thus the coincidence of MP and FBP frequencies results from offsetting core-size and substituent mixing effects.

The 600−1000 cm^{-1} region is particularly important for out-of-plane modes (see below). In this region there is good frequency correspondence for the in-plane modes of MP and FBP-X_8, although the intensity pattern is in better accord with

TABLE 3: Predicted Out-of-Plane Mode Frequencies and Intensities for the FBP-X$_8$ Model, and Mode Correlation with NiOEP

symm D_{4h}/D_{2h}	assign γ_i	NiOEP exp^a	NiOEP SQM-DFT^b	FBP-X$_8$	I_{RR} RUF-γ_{14}	symm D_{4h}/D_{2h}	assig γ_i	NiOEP exp^a	NiOEP SQM-DFT^b	FBP-X$_8$ B_{1u}	SAD-γ_{18}	DOM-γ_9	symm D_{4h}/D_{2h}	assign γ_i	NiOEP exp^a	NiOEP SQM-DFT^b	B_{2g}	I_{RR} WAV(X)-γ_{26}	B_{3g}	I_{RR} WAV(Y)-γ_{26}
A_{1u}/A_u	1	750	750	712	3.85	A_{2u}/B_{1u}	4	844	836	841	0.02	0.40	$E_g/B_{2g(3g)}$	NH			649	8.50		
	2	[346]	542	434	0.07		5	739	741	723	0.72	5.29		19	841	838	841	7.26	842	24.74
	3	[74]	59	159	0.02		6	360	362	768 (NH)	0.77	21.32		20	[731]	737	717	0.05	733	4.54
B_{1u}/A_u	10	853	840	843	72.05		7	284	271	385	0.02	0.27		21	656	729	699	1.36	711	0.02
	11	732	733	720	0.80		8	[108]	145	174	0.15	0.07		22	494	550	509	2.89	506	2.17
	12	612	438	552	4.91		**9**	[32]	41	**62**	0.03	**0.07**		23	254	218	357	1.52	356	0.73
	13	[130]	264	255	0.23	B_{2u}/B_{1u}	15	704	710	691	0.72	0.07		24	230	287	277	0.00	287	0.30
	14	[44]	3	**53**	**13.70**		16	270	240	361	0.21	0.00		25	[91]	87	139	0.34	155	0.44
							17	127	110	301	0.02	0.20		**26**	[63]	44	**88**	**4.13**	**90**	**2.68**
							18	[30]	11	**36**	**1.13**	0.00								

[a,b]As in Table 1. [c] RR intensities, relative to ν_4, computed for a 1 Å distortion along the indicated coordinates: γ_{14} (ruffling), γ_{18} (saddling), γ_9 (doming), γ_{26} (waving).

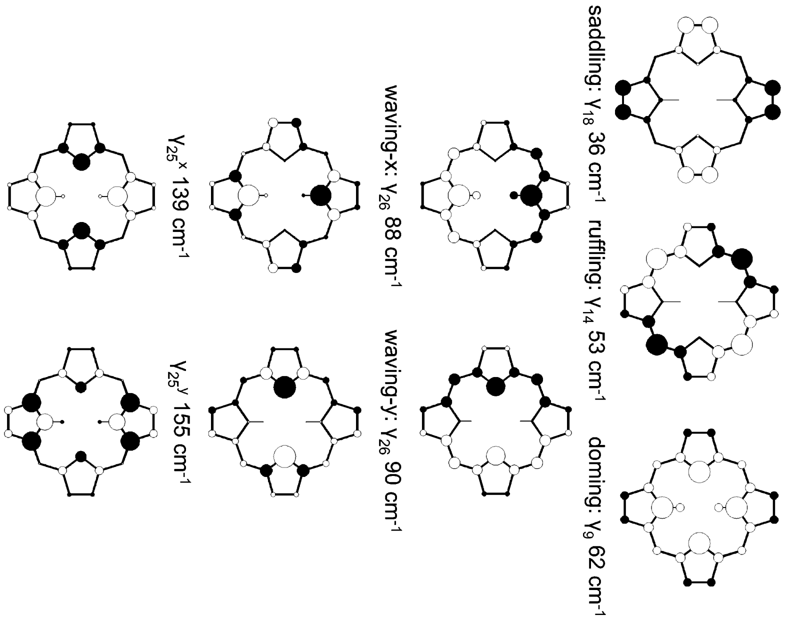

Figure 5. Selected oop mode eigenvectors of FBP-X$_8$.

experiment for the computed MP spectrum, as might be expected. However, the MP computation produces too much intensity for infrared-active modes, which are Raman-forbidden in D_{4h} or D_{2h} symmetry ($B_{2u(3u)}$; see Table 2). These modes are absent in the computed FBP-X$_8$ spectrum, but the substituent asymmetry in MP induces RR intensity. Experimentally, the effect is modest; this can be seen in the moderate intensity of the experimental band at 981 cm^{-1}, corresponding to ν_{45}. The computation, however, yields a ν_{45} band that is stronger than ν_7, experimentally the strongest band in the low-frequency region.

The low-frequency region MP spectrum is considered further below.

Out-of-Plane Intensities and Porphyrin Distortion. *Out-of-Plane Frequencies.* Table 3 compares the DFT-SQM frequencies of the FBP-X$_8$ out-of-plane (oop) modes with those of NiOEP. Again the correlations are easily recognizable, and the splittings occasioned by the symmetry lowering to D_{2h} ($E_g \rightarrow B_{2g}$, B_{3g}) are small. Replacing the Ni of NiOEP with the two protons of FBP-X$_8$ introduces two oop NH bends near 700 cm^{-1}, one of which replaces γ_6 (B_{1u}), and the other of which (B_{2g}) is an additional mode. The remaining modes show a close correspondence with those of NiOEP.

As long as the porphyrin is flat, there is no mechanism for activating oop modes in Raman spectra that are resonant with the dominant in-plane electronic transitions. But some NiOEP oop modes have been identified in RR spectra[12,39] (Table 3), because the porphyrin skeleton is distorted to accommodate the short Ni−N distance. The oop intensities have been computed in earlier studies of Ni-pophine[18] and Ni-tetraphenylporphine,[17] whose DFT-optimized geometries were distorted. The computed intensities were found to be qualitatively consistent with experiment.

TABLE 4: Predicted Frequencies and RR Intensities for In-Plane and Out-of-Plane Modes

assign	FBP-X8			MP				NMP		
ν_i/γ_i	calc	$I_{\mathrm{Flat}}{}^{a}$	$I_{\mathrm{NMP}}{}^{b}$	$^{\mathrm{Free}}$exp	calc	$I_{\mathrm{Flat}}{}^{a}$	$I_{\mathrm{NMP}}{}^{b}$	exp	calc	I[a]
ν_8	348	5.7	5.6	324	315[a]	7.7	3.9	332	331[a]	4.7
$\boldsymbol{\gamma_{23}}$	**356**	**0.0**	**0.0**		**362**	**0.0**	**0.1**		**317[a]**	**6.1**
$\boldsymbol{\gamma_{22}}$	**506**	**0.0**	**0.1**		**535[b]**	**0.4**	**0.4**	**~500**	**562[b]**	**2.5**
ν_7	677	4.0	3.9	661	657	20.0	21.6	663	655	21.0
ν_{48}	637	0.0	0.0		677	2.5	8.0	680	676	1.7
$\boldsymbol{\gamma_{15}}$	**691**	**0.0**	**0.5**		**682**	**0.1**	**4.3**		**694**	**1.2**
$\boldsymbol{\gamma_{5}}$	**723**	**0.0**	**1.9**		**718**	**0.3**	**1.1**		**707**	**0.7**
ν_{15}	738	0.8	1.0	736	740	5.9	6.3	738	734	9.4
ν_{16}	731	0.2	0.3		680	1.9	1.0		735[c]	6.9
$\boldsymbol{\gamma_{20}}$	**733**	**0.0**	**1.9**		**694**	**0.3**	**2.5**		**740[c]**	**3.6**
ν_6	804	3.2	3.2	768	768	5.0	7.2	759	764	11.7
$\boldsymbol{\gamma_{6,\mathrm{NH}}}$	**768**	**0.0**	**4.3**		**759**	**5.4**	**5.9**		**771**	**0.3**
$\boldsymbol{\gamma_{19}}$	**841**	**0.0**	**0.3**		**856**	**0.0**	**0.0**	**862**	**849**	**7.2**
ν_{46}	946	0.0	0.0		793	2.9	3.8		791	0.2
ν_{45}	962	0.0	0.0	981	978	30.8	27.8	982	971	22.7
ν_5	1112	11.8	11.3	1120	1189	26.8	34.7	1118	1197	29.3
ν_{14}	1125	4.0	4.2		1093	5.6	10.3		1099	9.5
ν_{13}	1235	0.1	6.9	1225	1223	26.8	31.4	1224	1222	26.9
ν_4	1374	100.0	100.0	1370	1363	100.0	100.0	1363	1362	100.0
ν_{12}	1406	6.8	6.9		1381	4.4	3.5	1369	1374	3.0
ν_3	1496	2.9	2.8	1486	1463	19.3	16.9	1472	1461	16.7
ν_{11}	1581	3.2	2.2		1502	9.9	10.8	1551	1498	16.3
ν_2	1644	5.7	5.9	1551	1594	22.2	24.8	1555	1587	33.8
ν_{10}	1679	1.5	1.6	1619	1604	17.2	14.7	1605	1602	12.3

[a] Predicted intensities for the unconstrained molecule: flat for FBP-X_8 and MP, 32° pyrole tilting for NMP. [b] Predicted intensity when constrained to NMP porphyrin geometry.

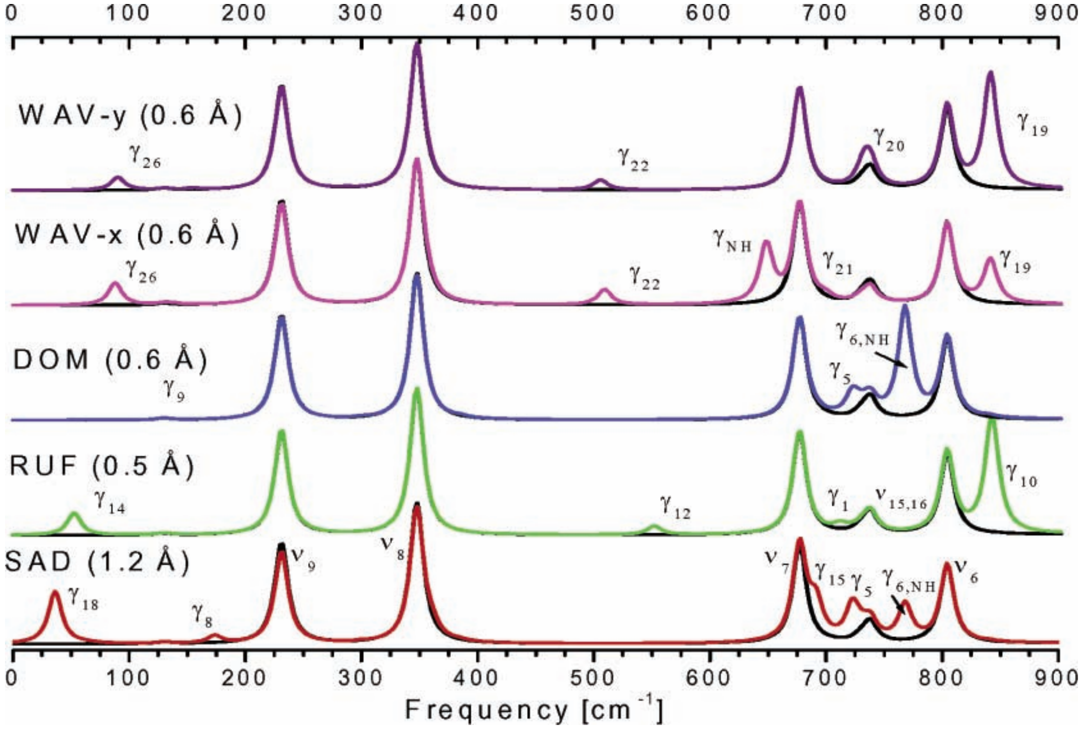

Figure 6. Computed FBP-X_8 RR spectra showing the effects (in color) of distortion along the indicated coordinate (displacements indicated in parantheses).

Modeling Out-of-Plane Constraints with FBP-X_8. We seek to model the effects of external constraints, e.g., nonbonded forces in proteins, on the oop RR intensities, and have used FBP-X_8 for this purpose. The most intuitive approach is to adopt Shelnutt's normal-coordinate structural decomposition,[41] in which a given distortion can be constructed from the eigenvectors of a set of low-frequency oop modes. Using a heme skeleton (24 atoms) reference structure, Shelnutt showed that the oop distortions reported for many heme protein crystal structures can be approximated by a linear combination of ruffling (ruf), doming (dom), saddling (sad), and waving (wav) distortions,[42] represented by the eigenvectors of the lowest frequency B_{1u}, A_{2u}, B_{2u}, and E_g modes. In D_{2h} symmetry, ruf is A_u, dom and sad are both B_{1u}, and the two wav componenets are B_{2g} (wav-*x*) and B_{3g} (wav-*y*) (see bold entries in Table 3 and eigenvectors illustrated in Figure 5).

Table 3 lists computed RR intensities for a FBP-X_8 molecule that has been constrained to distort by 1 Å along the indicated distortion coordinate. The coordinate displacement is the square-root of the sum of atomic displacements, d_j projected on the eigenvector e_j: $D_j = (\Sigma_{ij} d_i e_j)^{1/2}$. (We note that Jentzen et al.[41] limited the sum to the 24-atom porphyrin skeleton, whereas we have also include the substituent H and X atoms.) As expected, significant intensity is predicted for the mode along which the displacement occurs, but even greater intensification is computed for selected higher frequency modes (although the lowest frequency mode intensities are known to be undercomputed because of the neglect of the Kramers–Kronig correction,[17,18] as noted above). The different distortion coordinates have quite different effects on the various oop intensities, as illustrated in Figure 6, where computed spectra for the five displacements are superimposed on the calculated spectrum of flat FBP-X_8. In this case the coordinate displacement has been adjusted to the indicated values to obtain comparable overall enhancement of oop modes, because the displacement sensitivity is quite different for the different coordinates.

Because bands below 200 cm^{-1} are difficult to observe experimentally, the main differences are expected to appear in the 600–900 cm^{-1} region. Doming should be marked by strong intensification of the γ_6 NH bend (768 cm^{-1}), whereas saddling uniquely intensifies γ_{15}, a shoulder on the side of the ν_7 band (677 cm^{-1}). This is of considerable interest, because a growing ν_7 shoulder is the principal RR signature of MP bound to the 7G12 ferrochelatase antibody, which is the subject of another paper.[20]

Spectral crowding makes some of the differences hard to identify. For example the most strongly activated bands for ruf and wav distortions, γ_{10} and γ_{19}, respectively, are essentially coincident (843 and 842 cm^{-1}) and would not distinguish between these distortions. On the other hand, enhancement of γ_{NH} (649 cm^{-1}) is unique to the wav-*x* distortion. The reason is that the *x*-direction was chosen to coincide with the N–H···H–N direction, whereas the *y*-axis is the N···N direction. Thus γ_{NH} signals out-of-plane motion of the N–H vectors.

Testing the Model: NMP. To assess the value of the FBP-X_8 mxodel, we examined the RR spectrum of the intrinsically distorted porphyrin, *N*-methylmesoporphyrin (NMP), in which one of the pyrrole proton is replaced by a methyl group (Figure 1). The steric bulk of the methyl group excludes it from the central cavity of the porphyrin, and the pyrrole ring to which it is attached is tilted out of the plane by 32°.

RR spectra were computed for the equilibrium structures of NMP and MP. Structural parameters computed for NMP are compared (Table 1) with the only structurally characterized analogue, *N*-methyltetrakis(*p*-bromophenyl)porphyrin.[43] Despite the very different substituents, the agreement is quite good. Computed spectra are compared with the experimental spectra in Figure 7 (top and bottom). The frequencies and computed intensities are given in Table 4, where assignments are indicated by comparison with FBP-X_8. The experimental NMP spectrum shows subtle but distinctive differences, relative to that of MP, and the computed spectra provide a reasonable explanation of these differences. Oop modes are activated even in MP, despite its porphyrin ring being flat, because of the out-of-plane orientation of the ring substituents. However, the predicted intensities are low, except for $\gamma_{6,NH}$ (759 cm^{-1}), which overlaps with ν_6 (768 cm^{-1}) to produce a broad band, seen also in the experimental MP spectrum. (As noted above, the ν_{45} intensity is overestimated by the computation, and two other infrared modes, ν_{46} and ν_{48} are also seen to be exaggerated.) For NMP, additional activation of two oop modes, γ_{15} (694 cm^{-1}) and γ_{19} (849 cm^{-1}) is clearly seen in both computed and experimental spectra, and the gap between ν_{15} and $\nu_6/\gamma_{6,NH}$ is filled in by γ_{20} (740 cm^{-1}). We note that the intensification of the ν_{15} peak is attributable to overlap with ν_{16}, which is shifted up (735 cm^{-1}) relative to its position (680 cm^{-1}) in MP.

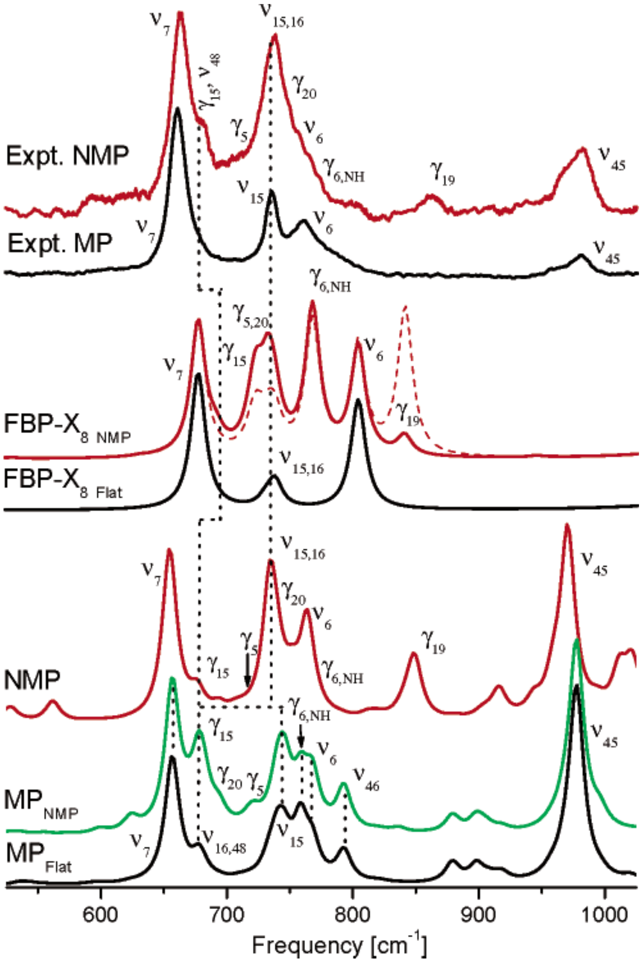

Figure 7. Experimental RR spectra for MP and NMP compared with computed spectra. Including constrains to the NMP porphyrin geometry.

The 32° pyrrole tilt of NMP does not correspond to any one of the D_{4h} distortion modes, but one can decompose the NMP structure into a linear combination of the various distortion coordinates. We did this using a complete set of FBP-X_8 oop modes, thereby encompassing the NMP skeleton, minus the pyrrole methyl group and the substituent atoms beyond the C atoms attached to the ring. The result is shown in Figure 8 as a bar diagram representing the coordinate displacements, as defined above, for all the oop modes.

As expected, the lowest frequency modes are the major contributors, and the coordinates defined by Shelnutt,[1] especially sad, dom and wav, account for much of the distortion. However, contributions of the numerous other coordinates are far from negligible. In particular, the B_{1u} mode, γ_8, and the B_{3g} mode γ_{25} (eigenvectors in Figure 5), contribute substantially. Their frequencies are below 200 cm^{-1}, so the distortion energies are not prohibitive.

We then calculated RR spectra of FBP-X_8 constrained to the NMP geometry using the derived linear combination of distortion coordinates (Figure 7, red spectra). When the computation was limited to contributions from the lowest frequency distortion coordinates, strong activation was obtained for γ_{19}, γ_6, γ_5, and γ_{20}, as expected from the large wav, dom, and sad distortions. However, when all the oop coordinate displacements were included, the γ_{19} intensity was greatly reduced, whereas γ_5 and γ_{20} activation was augmented. This intensity pattern is in better accord with the experimental spectrum of NMP. Thus cutting

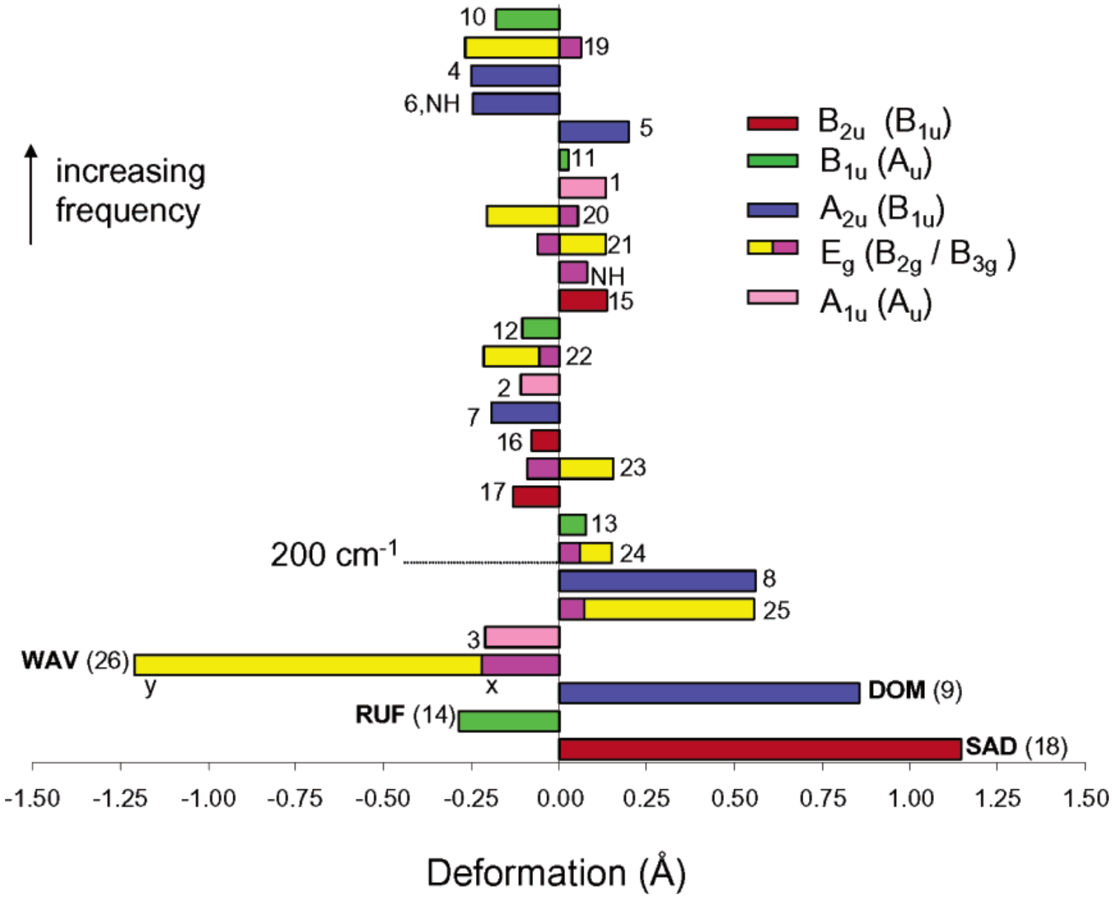

Figure 8. Extent of displacement along the indicated oop coordinates (see Table 2 for mode numbering) for a FBP-X_8 structure, which is constrained to the NMP porphyrin geometry.

off the distortion coordinates at just the lowest frequency set distorts the activation pattern significantly. Table 4 gives computed intensities for the principal oop and in-plane modes, using the complete set of displacement coordinates for the constrained FBP-X_8 structure (column labeled I_{NMP}).

We considered alternative tautomers of FBP-X_8. Although a trans arrangement of the NH protons is expected to be more stable than the cis arrangement, there are two trans alternatives in the NMP-constrained structure, with the protons on rings A and C, or on B and D. The computed spectra of these tautomers are compared in Figure 7 (green and red spectra). As expected from the wav-*x* computation in the preceding section, the A,C spectrum is expected to show strong activation of γ_{NH}, below ν_7. Because NMP itself has a methyl group, not a proton, on ring A, this feature is not seen in the experimental NMP spectrum. Curiously, strong activation of the infrared modes ν_{45} and ν_{48} is also seen in the computed A,C, but not B,D, spectrum. The tautomer sensitivity of the RR spectrum gives promise of locating the protons in distorted free-base porphyrins, information that is not readily available from protein crystal structures.

Table 4 also lists computed intensities for MP when it was constrained to the NMP structure. This computed spectrum is a key feature of our ferrochelatase antibody study.[20]

Conclusions

Our results show that CIS produces excited state gradients, within the four-orbital model of $\pi-\pi^*$ excitations, which do a good job of predicting the RR intensity pattern for free-base porphyrins. However, it is important to recognize the different levels of theory applied to the ground (DFT) and excited (CIS) states, and to correct for the associated shift between the potential energy surfaces. Gradients calculated without this correction give completely erroneous RR intensities.

An additional complication arises from the splitting of the resonant excited state into separate (*x*- and *y*-polarized) components, which interfere constructively and destructively in establishing the RR intensities. Although the weighting factors could be evaluated experimentally, we have found it convenient to adjust their ratio to fit the observed RR intensity pattern. Because of the near-degeneracy of the B_x and B_y components, a 1:1 weighting serves adequately to reproduce the experimental spectra; modest deviations from this ratio have small effects on the intensity pattern.

The artificial molecule FBP-X_8 is helpful in modeling the RR spectra of physiological porphyrins, which have carbon substituents attached to the C_b atoms. The heavy X pseudoatoms capture the substituent kinematics approximately, while maintaining 4-fold symmetry for the porphyrin skeleton. The symmetry permits separate classification of the canonical oop distortion coordinates: doming, saddling, ruffling and waving. When they are applied to FBP-X_8, RR activation is predicted, not only for the canonical modes (which are too low in frequency to be detected in RR experiments) but also for other modes in the same symmetry class. Thus the RR spectra permit a ready choice among the distortion coordinates, provided only one of them is expressed in the structure.

In actuality, distorted structures are more complicated but can be represented approximately by a linear combination of the canonical coordinates. The RR spectrum can be constructed accordingly. However, the use of only the canonical coordinates, i.e., the lowest frequency mode of each of the symmetry classes, can leave important contributions out of account. Thus constraining the structure of FBP-X_8 to the distorted porphyrin skeleton of NMP yielded a normal coordinate decomposition with significant contributions from oop modes other than the lowest frequency ones. Omission of these noncanonical contributions considerably altered the computed oop mode RR intensity pattern. The modeled RR spectrum is quite sensitive to the accuracy of the normal mode representation of the oop distortion of the porphyrin.

Additionally, the spectrum is sensitive to the placement of the protons in free-base porphyrins, if the pyrrole are differentially tilted. FBP-X_8 showed strong activation of a characteristic NH oop mode only when the pyrrole ring being tilted was protonated. Thus the RR spectrum may be useful in determining the protonation sites in distorted free-base porphyrins.

Acknowledgment. We thank Drs. Candace Coyle and Swarnalatha Venkateshrao for kindly recording the Raman spectra of FBP, MP, and NMP. The work was supported by NIH grant GM 33576 from the National Institute of General Medical Sciences.

References and Notes

(1) Shelnutt, J. A.; Song, X. Z.; Ma, J. G.; Jia, S. L.; Jentzen, W.; Medforth, C. J. *Chem. Soc. Rev.* **1998**, *27*, 31.

(2) Jordan, P. M. *Curr. Opin. Struct. Biol.* **1994**, *4*, 902.

(3) Dailey, H. A. In *Biosynthesis of Heme and Chlorophylls*; Dailey, H. A., Ed.; McGraw-Hill Publishing Co.: New York, 1990; p 123.

(4) Karger, G. A.; Reid, J. D.; Hunter, C. N. *Biochemistry* **2001**, *40*, 9291.

(5) Lavallee, D. K. In *Mechanistic Princeiples of Enzyme Activity*; Liebman, J. F., Greeberg, A., Eds.; VCH: New York, 1988; p 279.

(6) Dailey, H. A. In *Mechanisms of Metallocenter Assembly*; Hausinger, R. P., Eichorn, G. C., Marzilli, C. G., Eds.; VCH: New York, 1996; p 77.

(7) Sparks, L. D.; Chamberlain, J. R.; Hsu, P.; Ondrias, M. R.; Swanson, B. A.; Demontellano, P. R. O.; Shelnutt, J. A. *Inorg. Chem.* **1993**, *32*, 3153.

(8) Dailey, H. A.; Fleming, J. E. *J. Biol. Chem.* **1983**, *258*, 11453.

(9) Cochran, A. G.; Schultz, P. G. *Science* **1990**, *249*, 781.

(10) Tsai, H. H.; Simpson, M. C. *J. Phys. Chem. A* **2004**, *108*, 1224.

(11) Brennan, T. D.; Scheidt, W. R.; Shelnutt, J. A. *J. Am. Chem. Soc.* **1988**, *110*, 3919.

(12) Alden, R. G.; Crawford, B. A.; Doolen, R.; Ondrias, M. R.; Shelnutt, J. A. *J. Am. Chem. Soc.* **1989**, *111*, 2070.

(13) Czernuszewicz, R. S.; Li, X. Y.; Spiro, T. G. *J. Am. Chem. Soc.* **1989**, *111*, 7024.

(14) Jentzen, W.; Unger, E.; Karvounis, G.; Shelnutt, J. A.; Dreybrodt, W.; Schweitzer Stenner, R. *J. Phys. Chem.* **1996**, *100*, 14184.

(15) Hoard, J. L. *Science* **1971**, *174*, 1295.

(16) Kozlowski, P. M.; Rush, T. S.; Jarzecki, A. A.; Zgierski, M. Z.; Chase, B.; Piffat, C.; Ye, B. H.; Li, X. Y.; Pulay, P.; Spiro, T. G. *J. Phys. Chem. A* **1999**, *103*, 1357.

(17) Rush, T. S.; Kozlowski, P. M.; Piffat, C. A.; Kumble, R.; Zgierski, M. Z.; Spiro, T. G. *J. Phys. Chem. B* **2000**, *104*, 5020.

(18) Rush, T. S.; Kumble, R.; Mukherjee, A.; Blackwood, M. E.; Spiro, T. G. *J. Phys. Chem.* **1996**, *100*, 12076.

(19) Kumble, R.; Rush, T. S.; Blackwood, M. E.; Kozlowski, P. M.; Spiro, T. G. *J. Phys. Chem. B* **1998**, *102*, 7280.

(20) Venkateshrao, S.; Yin, J.; Jarzecki, A. A.; Schultz, P. G.; Spiro, T. G. *J. Am. Chem. Soc.* **2004**, *126*, 16361.

(21) Hizhnyakov, V.; Tehver, I. *Phys. Status Solidi* **1967**, *21*, 755.

(22) Chan, C. K.; Page, J. B. *J. Chem. Phys.* **1983**, *79*, 5234.

(23) Savin, F. A. *Opt. Spektrosk.* **1965**, *19*, 555.

(24) Warshel, A.; Dauber, P. *J. Chem. Phys.* **1977**, *66*, 5477.

(25) Heller, E. J.; Sundberg, R. L.; Tannor, D. *J. Phys. Chem.* **1982**, *86*, 1822.

(26) Lee, S.-Y.; Heller, E. J. *J. Chem. Phys.* **1979**, *71*, 4777.

(27) Frisch, M. J.; Trucks, G. W.; Schlegel, H. B.; Scuseria, G. E.; Robb, M. A.; Cheeseman, J. R.; Zakrzewski, V. G.; Montgomery, J. A., Jr.; Stratmann, R. E.; Burant, J. C.; Dapprich, S.; Millam, J. M.; Daniels, A. D.; Kudin, K. N.; Strain, M. C.; Farkas, O.; Tomasi, J.; Barone, V.; Cossi, M.; Cammi, R.; Mennucci, B.; Pomelli, C.; Adamo, C.; Clifford, S.; Ochterski, J.; Petersson, G. A.; Ayala, P. Y.; Cui, Q.; Morokuma, K.; Malick, D. K.; Rabuck, A. D.; Raghavachari, K.; Foresman, J. B.; Cioslowski, J.; Ortiz, J. V.; Baboul, A. G.; Stefanov, B. B.; Liu, G.; Liashenko, A.; Piskorz, P.; Komaromi, I.; Gomperts, R.; Martin, R. L.; Fox, D. J.; Keith, T.; Al-Laham, M. A.; Peng, C. Y.; Nanayakkara, A.; Gonzalez, C.; Challacombe, M.; Gill, P. M. W.; Johnson, B. G.; Chen, W.; Wong, M. W.; Andres, J. L.; Head-Gordon, M.; Replogle, E. S.; Pople, J. A. *Gaussian 98*, revision A.7; Gaussian, Inc: Pittsburgh, PA, 1998.

(28) Rauhut, G.; Pulay, P. *J. Am. Chem. Soc.* **1995**, *117*, 4167.

(29) Baker, J.; Jarzecki, A. A.; Pulay, P. *J. Phys. Chem. A* **1998**, *102*, 1412.

(30) Jarzecki, A. A.; Kozlowski, P. M.; Pulay, P.; Ye, B. H.; Li, X. Y. *Spectrochim. Acta A* **1997**, *53*, 1195.

(31) Foresman, J. B.; Head-Gordon, M.; Pople, J. A.; Frisch, M. J. *J. Phys. Chem.* **1992**, *96*, 135.

(32) Jarzecki, A. A.; Spiro, T. G. *J. Raman Spectrosc.* **2001**, *32*, 599.

(33) Gouterman, M. *J. Mol. Spectrosc.* **1961**, *6*, 138.

(34) Gouterman, M.; Wagniere, G. H.; Snyder, L. C. *J. Mol. Spectrosc.* **1963**, *11*, 108.

(35) Kozlowski, P. M.; Jarzecki, A. A.; Pulay, P. *J. Phys. Chem.* **1996**, *100*, 7007.

(36) Kozlowski, P. M.; Jarzecki, A. A.; Pulay, P.; Li, X. Y.; Zgierski, M. Z. *J. Phys. Chem.* **1996**, *100*, 13985.

(37) Stoll, L. K.; Zgierski, M. Z.; Kozlowski, P. M. *J. Phys. Chem. A* **2002**, *106*, 170.

(38) Stoll, L. K.; Zgierski, M. Z.; Kozlowski, P. M. *J. Phys. Chem. A* **2003**, *107*, 4165.

(39) Li, X. Y.; Czernuszewicz, R. S.; Kincaid, J. R.; Spiro, T. G. *J. Am. Chem. Soc.* **1989**, *111*, 7012.

(40) Parthasarathi, N.; Hansen, C.; Yamaguchi, S.; Spiro, T. G. *J. Am. Chem Soc.* **1987**, *109*, 3865.

(41) Jentzen, W.; Song, X. Z.; Shelnutt, J. A. *J. Phys. Chem. B* **1997**, *101*, 1684.

(42) Scheidt, W. R.; Lee, Y. J. *Struct. Bonding* **1987**, *64*, 1.

(43) Lavallee, D. K.; Anderson, O. P. *J. Am. Chem. Soc.* **1982**, *104*, 4707.

(44) Chen, B. M. L.; Tulinsky, A. *J. Am. Chem. Soc.* **1972**, *94*, 4144–4151.